Available online at www.sciencedirect.com
ScienceDirect
Acta Materialia 55 (2007) 635–646
Acta MATERIALIA
www.actamat-journals.com

Nanoscratching of nylon 66-based ternary nanocomposites

Aravind Dasari, Zhong-Zhen Yu *, Yiu-Wing Mai

Centre for Advanced Materials Technology (CAMT), School of Aerospace, Mechanical and Mechatronic Engineering J07, University of Sydney, Sydney, NSW 2006, Australia

Received 29 May 2006; received in revised form 27 July 2006; accepted 22 August 2006
Available online 22 November 2006

Abstract

The nanoscratch behavior of nylon 66/SEBS-g-MA/clay ternary nanocomposites produced by different blending protocols with contrasting microstructures is studied by using atomic force and transmission electron microscopy. A standard diamond Berkovich indenter is used for scratching and a low load of 1 mN, along with a low sliding velocity of 1 μm s^{-1}, are employed for this purpose. It is shown that in order to resist penetration it is more important to have exfoliated clay in the continuous nylon matrix during nanoscratching than to have the clay in the dispersed soft rubber domains. The results obtained also explain the preferred usage of ternary nanocomposites compared to binary nanocomposites, particularly nylon 66/exfoliated clay nanocomposites. This research extends current basic knowledge and provides new insights on the nature of nanoscale processes that occur during nanoscratching of polymer nanocomposites. Critical questions are raised on the relationships between the penetration depth and material deformation and damage left behind the moving indenter.

Keywords: Nanoscratch; Nanocomposite; AFM; Exfoliation; Nylon

1. Introduction

Recent advances in miniaturization of polymer components for nanotechnology applications require the characterization (hardness, elastic modulus and yield stress) of their surface and near-surface mechanical properties as these properties have been shown to govern the performance of such components. For this purpose, depth-sensing instruments, in particular nanoindentation, are being widely used to probe the mechanical properties of a number of polymeric materials, including polyvinylchloride (PVC), poly(methyl-methacrylate) (PMMA), poly(ethylene terephthalate) (PET), poly(ethylene oxide) (PEO), nylon 6, nylon 66 [1–9] and polymer nanocomposites, such as PEO/clay [10], nylon 66/clay [11,12], nylon 12/clay [13], epoxy/carbon nanotube (CNT) [14], nylon 6/CNT [15], nylon 6/clay [16] and photopolymer/SiO_2 [17] nanocomposites. This method relies on the local deformation induced by an indenter of known geometry and applied load [18]. It has been shown that, in general, with increasing filler loading, the resistance to indentation of the nanocomposites gradually increases.

However, for certain nanotechnology applications, such as magnetic storage systems and micro-electromechanical systems, particularly with moving parts and components subject to intermittent or continuous contact, wear rates must be almost zero for efficient functioning. For other applications, such as nanomachining, nanopatterning and nanofabrication, very small applied loads (μN and nN) are used and, like mechanical scratching, they require material surfaces to deform at the nanoscale and deliberate removal of materials [19–21]. Hence, the nanoscratching technique may also be used as a tool to determine the performance of a material and hence assess its suitability for various applications.

Nanoscratching has been extensively used to evaluate the scratch, wear and friction behaviors of polymers [22–25], polymer microcomposites [26,27], thin films [28,29], magnetic coatings and electronic materials

* Corresponding author. Fax: +61 2 93513760.
E-mail address: zhongzhen.yu@aeromech.usyd.edu.au (Z.-Z. Yu).

1359-6454/$30.00
doi:10.1016/j.actamat.2006.08.056

[30,31], and to a lesser extent polymer-based nanocomposites [32–34] that are used as optical clear coatings. In the case of simple polymers (epoxies, polycarbonate and PMMA), nanoscale scratching results suggest that under identical testing conditions, the surface damage encountered is material specific [22]. More importantly, the mechanical properties of polymers (e.g. ductility and modulus) are found to affect the surface damage observed and the deformation mechanism involved when the polymers are scratched at the nanoscale. Under the same normal scratching load, shallower grooves are formed on higher-modulus polymers, and polymers plastically deform if their surface ductility is higher.

Very few studies have focused on scratch damage in polymer nanocomposites at the nanoscale. Li et al. [32] used atomic force microscopy (AFM) to characterize the scratch morphology, depth and width of scratch tracks in nanoscale alumina-filled gelatin composite films. They showed that the scratching resistance was greatly improved with the addition of as-received Al_2O_3 nanoparticles and this improvement was attributed to the increase in yield stress and modulus caused by the addition of filler owing to its load-bearing capability. In other studies [33,34], it was also shown that nanoscale fillers could reduce the scratch depth in both thermoplastic and thermoset composites by 50% compared to their unfilled and micron-size-filled counterparts. However, in all these previous investigations, little attention was paid to the deformation and subsequent morphology of the surface and subsurface materials within the scratch track left behind the moving indenter tip. But this basic knowledge is critical to understanding and controlling material damage and material removal. Moreover, only a few attempts have been made to model the stress fields induced by different slider geometries due to the complexities involved in scratch damage, particularly for polymer nanocomposites at the nanoscale. Thus, no explicit correlations between material parameters and scratch damage are currently available. The main aim of this study is to understand the structure–scratch resistance relationship by revealing the nanoscale nature of intimate contact. We have used AFM and transmission electron microscopy (TEM) during nanoscratching of nylon 66-based ternary nanocomposites with contrasting microstructures. Nanoscratching was performed with a standard diamond Berkovich indenter at a low load of 1 mN and a slow sliding speed of 1 $\mu m\,s^{-1}$. To the best of our knowledge, this is the first study of nanoscratch damage in polymer nanocomposites based on rigid clay and/or soft rubber as nano-additives. It is expected that experimental evidence of the nanoscratch damage mechanisms obtained will help us to develop models to predict material removal and design scratch/wear-resistant polymers with nano-additives.

As the interfaces between fillers and matrix in a polymer nanocomposite constitute a very high volume fraction of the bulk material, polymers often show improved mechanical properties if they possess a multicomponent, phase-separated morphology at the nanoscale [35]. From the tribological viewpoint, the major benefit of these polymer nanocomposites relative to micro-sized particle composites is that material removal is expected to be less as the nano-additives are of a similar size to the segments of the surrounding polymer chains [36–39]. This is possible owing to the much greater surface area-to-volume ratio of the nano-additives, which is important for bonding the particle to the polymer matrix. In addition to the influence on the tribological performance of the composites, the nano-additives also change the crystallinity, microstructure, physical and mechanical properties of the polymer matrix [40]. Therefore, a basic understanding of the nanotribological mechanisms is critical for evaluation of the deformation of asperities, crack initiation and growth, material removal, etc.

In our previous study, to obtain a balance in mechanical properties, i.e. high stiffness/strength and high toughness, nylon 66-based ternary nanocomposites were synthesized with organoclay as the reinforcing agent and a soft elastomer, SEBS-g-MA, as the toughening agent [41,42]. In addition, the effect of blending sequence on these ternary nanocomposites was studied. Distinct differences in the microstructures were obtained depending on the blending protocol. We have also shown that the level of enhancement in fracture toughness of these ternary nanocomposites depends on the capability of different fillers to activate the plastic deformation mechanisms in the matrix and the blending protocol employed [43]. These mechanisms include: cavitation of SEBS-g-MA phase, stretching of the voided matrix material, interfacial debonding of SEBS-g-MA particles, debonding of the intercalated clay present inside the SEBS-g-MA phase, and delamination of intercalated clay platelets. It has also been shown that if the clay is embedded in the dispersed rubber particles, it has a negative influence on fracture toughness since this makes the rubber more rigid and reduces its capability to cavitate.

2. Experimental work

2.1. Preparation of materials

Nylon 66, a polyamide resin with a trade name of Vydyne® 21PC, was supplied by Monsanto. Organoclay with a cation exchange capacity of 90 mequiv/100 g (trade name Cloisite® 30B) was obtained from Southern Clay Products Inc. via Jim Chambers & Associates, Australia. More information on the experimental materials and extrusion conditions is given elsewhere [41]. Four blending protocols were adopted for the preparation of ternary nanocomposites:

N1 (nylon 66 + SEBS-g-MA + organoclay) (80/15/5) – indicates that nylon 66, SEBS-g-MA and organoclay were blended simultaneously;

N2 (nylon 66 + SEBS-g-MA) + organoclay (80/15/5) – indicates that nylon 66 was blended with SEBS-g-MA first and the nylon 66/SEBS-g-MA blend was then mixed with the organoclay later;
N3 (nylon 66 + organoclay) + SEBS-g-MA (80/5/15) – indicates that nylon 66 was reinforced with organoclay first and the nylon 66/organoclay nanocomposite was then blended with SEBS-g-MA later;
N4 nylon 66 + (SEBS-g-MA + organoclay) (80/15/5) – indicates that SEBS-g-MA was mixed with organoclay and then the SEBS-g-MA/organoclay master batch was blended with nylon 66 later.

In addition, pure nylon 66 (B0), nylon 66/organoclay (80/5) binary nanocomposite (B1) and nylon 66/SEBS-g-MA (80/15) binary blend (B2) were also prepared under identical conditions. The extrudates of all the samples were pelletized and dried at 90 °C under vacuum for 12 h before being injection molded using a SZ-160/80 NB (China). The temperatures at the barrel and the mold were maintained at 270 and 70 °C, respectively.

2.2. Mechanical testing

Nanoscratch tests were carried out on finely polished, injection-molded specimens using a depth-sensing UMIS nanoindentation system (CSIRO, Australia), capable of recording the lateral force. Experiments were performed using a Berkovich three-sided pyramidal diamond indenter with a nominal angle (defined by the tip axis and faces) of 65.3° and a nominal radius of curvature of ~182 nm. Nanoscratching was done with the face-on orientation of the indenter at a normal load of 1 mN and a sliding speed of 1 μm s^{-1}. The scratch length was set at 100 μm. In addition to the nanoscratch tests, nanoindentation tests were also carried out with the same indenter at different loads of 1 and 5 mN. At least five tests were carried out for each condition and all the tests were performed at ambient (22 ± 1 °C). The notched impact strength (J m^{-1}) was determined with an ITR-2000 instrumented impact tester according to ASTM D256 on the injection-molded rectangular bars machined with a 45° V-notch (and depth of 2.54 mm) and listed in Table 1.

2.3. Microscopic analysis

2.3.1. Transmission electron microscopy

To study the microstructures of the four ternary nanocomposites prepared by different blending sequences, ultra-thin sections ranging from 60 to 90 nm in thickness were cryogenically cut with a diamond knife in liquid nitrogen at –80 °C using a Leica Ultracut S microtome. Sections were collected on holey formvar/carbon-coated copper grids and carefully stained with osmium tetroxide (OsO_4) vapor to enhance the phase contrast between nylon 66, clay and SEBS-g-MA. Subsequently, the thin sections were observed using a Philips CM12 transmission electron microscope at an accelerating voltage of 120 kV.

2.3.2. Atomic force microscopy

Nanoscratch-tested specimens were examined by AFM to study the nature of nanoscale contact and the effect of microstructure on the deformation process. AFM was carried out using a Nanoscope (R) IIIa (Digital Instruments, Santa Barbara, CA) in the tapping mode. The tapping mode was preferred to the contact mode to prevent possible surface damage arising from continuous contact. All the scans were made at ambient conditions and the tip used was a tapping mode etched silicon probe (TESP). The scan parameters and AFM scan-leveling procedures were identical for all the studied composites to enable direct comparisons of images. Multiple images were taken at a number of locations along the scratch on each sample so as to ensure that the images were true representatives of the topography of the surface, and were not characteristics of artefacts.

2.3.3. Post-mortem TEM analyses

Cross-sections of the subsurface beneath the scratch track were prepared by cryo-ultramicrotoming, and TEM analyses were conducted on those sections to study the damage that had occurred in the plastic zone under the indenter for some selected samples.

Table 1
Mechanical and scratch properties of ternary nanocomposites (properties of pure nylon 66 (N0) are given as a base reference)

Specimen	Scratch penetration depth (nm)	Hardness (GPa)	Elastic modulus (GPa)	Notched impact strength (J m^{-1})	Bulk elastic modulus (GPa)
N0: pure nylon 66	310 ± 8	0.11 ± 0.01	1.35 ± 0.02	62.5 ± 3.3	2.95 ± 0.05
N1: (nylon 66 + organoclay + SEBS-g-MA)	250 ± 9	0.11 ± 0.014	1.43 ± 0.05	102.9 ± 10.6	2.54 ± 0.11
N2: (nylon 66 + SEBS-g-MA) + organoclay	305 ± 10	0.10 ± 0.015	1.12 ± 0.07	78.9 ± 3.9	2.53 ± 0.07
N3: (nylon 66 + organoclay) + SEBS-g-MA	210 ± 7	0.14 ± 0.008	1.82 ± 0.02	117.6 ± 16.3	2.65 ± 0.03
N4: nylon 66 + (SEBS-g-MA + organoclay)	365 ± 11	0.10 ± 0.02	0.99 ± 0.08	65.9 ± 3.9	2.63 ± 0.02

3. Results and discussion

3.1. Microstructure

In our previous paper [41], we have shown the differences in the microstructures of binary and ternary nanocomposites produced by different blending sequences. However, to clearly follow the nanoscratching results, it is appropriate to briefly review again these distinct differences in the microstructures of nylon 66/organoclay/SEBS-g-MA ternary nanocomposites (N1–N4). Before describing the microstructures of these ternary nanocomposites, it is important to note that in the binary nanocomposite (B1), the clay platelets are well dispersed and distributed; while in the binary blend (B2), use of a grafted maleic anhydride results in the formation of a graft copolymer (nylon 66-co-SEBS-g-MA) generated by the reaction of the grafted maleic anhydride (MA) with the nylon amine end groups during the melt-compounding process. This grafted copolymer strengthens the interface between the phases (nylon 66 and SEBS), reduces interfacial tension, and also provides steric stabilization that retards the coalescence of the dispersed phase [44], thereby forming stable, finely dispersed and homogenized rubber particles in B2.

TEM micrographs of the ternary nanocomposites, N1–N4, are shown in Fig. 1 [41]. Note that the rubber particles are intentionally stained very lightly so as to clearly identify even the fine clay layers present in rubber particles. In N1 and N2, it can be seen that the SEBS-g-MA particles are finely dispersed in the nylon 66 matrix. The presence of clay does not seem to have a significant influence on the dispersion quality of the SEBS-g-MA phase in these sequences. However, depending on the interaction of clay with nylon 66 matrix and SEBS-g-MA particles, the dispersion quality of clay varied. Because nylon 66 is more polar than SEBS-g-MA, silicate layers seems to be well dispersed in the former, whereas thick platelets of clay are evident in the latter. In addition, the percentage of clay seems to be distributed equally between the nylon 66 matrix and SEBS-g-MA phase in N1 and N2. In N3, most of the clay seems to be present in the nylon 66 matrix with good dispersion and distribution, which suggests that this blending sequence, i.e. preparing a binary nylon/clay nanocomposite first, and then blending with rubber, is the best route regarding the dispersion quality of clay. In contrast, N4 exhibits a completely different behavior from N3 and N1 or N2. Most of the clay is present in the SEBS-g-MA phase as clay is blended with rubber first. As indicated above, the relatively

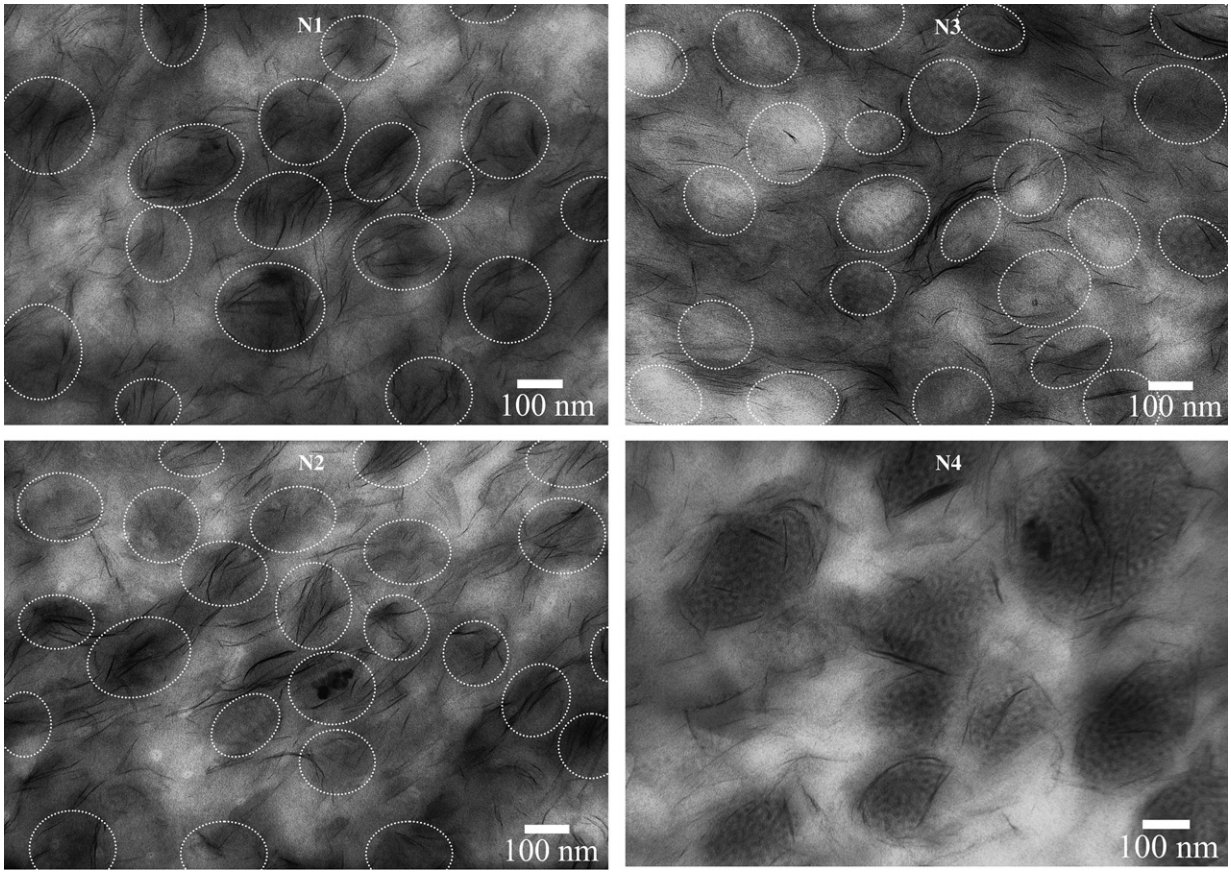

Fig. 1. TEM micrographs showing the dispersion quality of the fillers (clay and SEBS-g-MA particles) in ternary nylon 66/clay/SEBS-g-MA nanocomposites (N1–N4). The rubber particles, particularly in N1–N3, are stained very lightly to clearly identify even the fine clay layers embedded within. White dotted lines on the micrographs show approximate boundaries of the rubber particles.

low polar nature of SEBS-g-MA cannot exfoliate the silicate layers and results in an intercalated structure within the SEBS-g-MA phase. These contrasting differences in microstructures and the formation of distinct nanodomains in N1–N4 significantly affect the friction and the resistance to nanoscratching and nanoindentation (see below).

In our previous work [43], the state of exfoliation and dispersion of clay in nylon 66 matrix and SEBS-g-MA phase were also quantified as the presence of clay in rubber is shown to have a negative effect on the latter's cavitation ability and in turn on the fracture toughness of the nanocomposites. Table 2 shows the average length, thickness and aspect ratio of clay particles, together with the apparent content of clay in nylon 66 matrix and in SEBS-g-MA particles. It can be seen that the aspect ratio of clay particles in B1 (~50) is not very high and different to that under ideal conditions (several hundreds to thousands), which points to the practical difficulty of clay reinforcement. Compared to the binary nanocomposite, the aspect ratio of clay particles is even worse in the ternary nanocomposites.

Table 2
Quantification of clay particles[a] present in nylon 66 matrix and SEBS-g-MA particles in binary (B1) and ternary nanocomposites (N1–N4) using a semi-automated approach

Specimen	In nylon 66 matrix				In SEBS-g-MA particles			
	Average length of clay particles (nm)	Average thickness of clay particles (nm)	Aspect ratio of clay particles	Apparent % of clay (based on thickness)	Average length of clay particles (nm)	Average thickness of clay particles (nm)	Aspect ratio of clay particles	Apparent % of clay (based on thickness)
B1	95	1.9	50	100	–	–	–	–
N1	80	2.1	38	50	75	3.4	22	50
N2	81	2.2	37	46	65	3.2	20	54
N3	72	2.2	32	80	58	3.0	19	20
N4	71	3.2	22	18	70	4.7	15	82

[a] The sampling size for the calculation of these data is more than 1500 particles.

3.2. Nanoscratching

3.2.1. Friction

In Fig. 2, the average coefficient of friction is plotted against the scratch length for N1–N4 at a normal load of 1 mN and a scratching speed of 1 $\mu m\,s^{-1}$. The standard deviations plotted against the mean curve are for five tests. As the surface roughness and/or local slope of the asperities significantly influences the attractive forces (van der Waal/capillary forces) experienced by the indenter tip, which affects the lateral force/frictional force measured, samples are finely polished before the nanoscratching experiments in order to produce a roughness in the range 10–15 nm. Fig. 2 shows that the friction coefficients are different among N1–N4, suggesting variations in their deformation behaviors. N3 shows the highest average coefficient of friction; N4 the least.

3.2.2. Scratch morphology

Three-dimensional (3-D) AFM micrographs showing differences in the scratch behavior of the four ternary nanocomposites with distinctly different microstructures at identical scratch conditions (normal load of 1 mN and scratch velocity of 1 $\mu m\,s^{-1}$) at a field of view of 20×20 μm are given in Fig. 3. On the scratch tracks of all the ternary nanocomposites there are obvious plastically torn materials on the walls of the groove with a repeating pattern. In general, during nanoscratching, particularly at very low loads of the order of a few nN, this periodic pattern is observed in many materials. This has invariably been attributed to the "stick-slip" process [45] that occurs between the indenter tip asperities and the contacting material asperities. However, in the present case, no correlation exists when the length scale of the periodic pattern (shown in Fig. 3) is compared to their

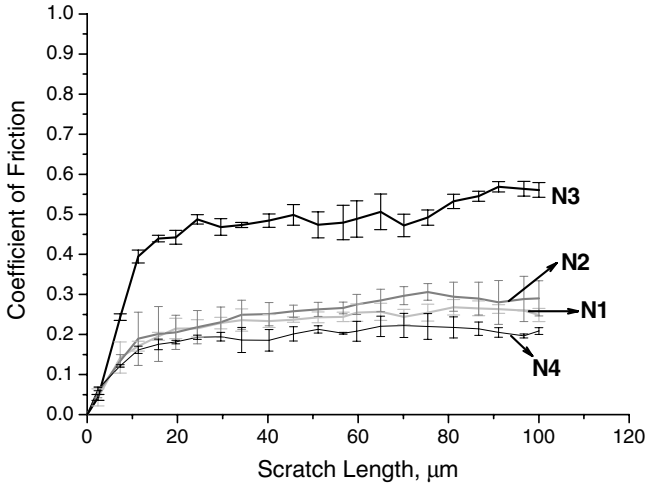

Fig. 2. Average coefficient of friction vs. scratch length for four ternary nanocomposites.

frictional coefficient data obtained along the scratch length (Fig. 2). Hence, the periodic pattern observed in these materials does not seem to relate to the "stick-slip" behavior. Instead, these repeated, periodic plastically torn materials on the sides of the groove within the scratch tracks may be a result of the sequential accumulation and release of the tangential force along the scratch length due to the viscoelastic nature of these polymers. This type of periodic pattern in the scratch tracks is also observed for many polymeric materials at higher applied normal loads [46–48]. Also, no evidence of cutting marks, chip formation and cracks within the scratch grooves could be found for any of the ternary nanocomposites (N1–N4); and it seems that the viscoelastic recovery at the rear end of the contact is accompanied by plastic plowing processes in front where the material is moved to the sides and pushed ahead of the moving indenter. However, there is little pile-up of material on both sides of the grooves, which may be due to the shape of the Berkovich indenter, the attack angle of which generally flattens the pile-ups, particularly at low loads [49]. This therefore results in more pronounced grooves. This behavior is clearly shown in the nylon 66/SEBS-g-MA soft blend (see below, Fig. 4). Furthermore, the size of contact is controlled by the compressive strength of the surface, resisting the motion of the indenter in front. The tensile stresses on the surface just behind the indenter control the formation of surface cracks, while in the shear-stress-dominant

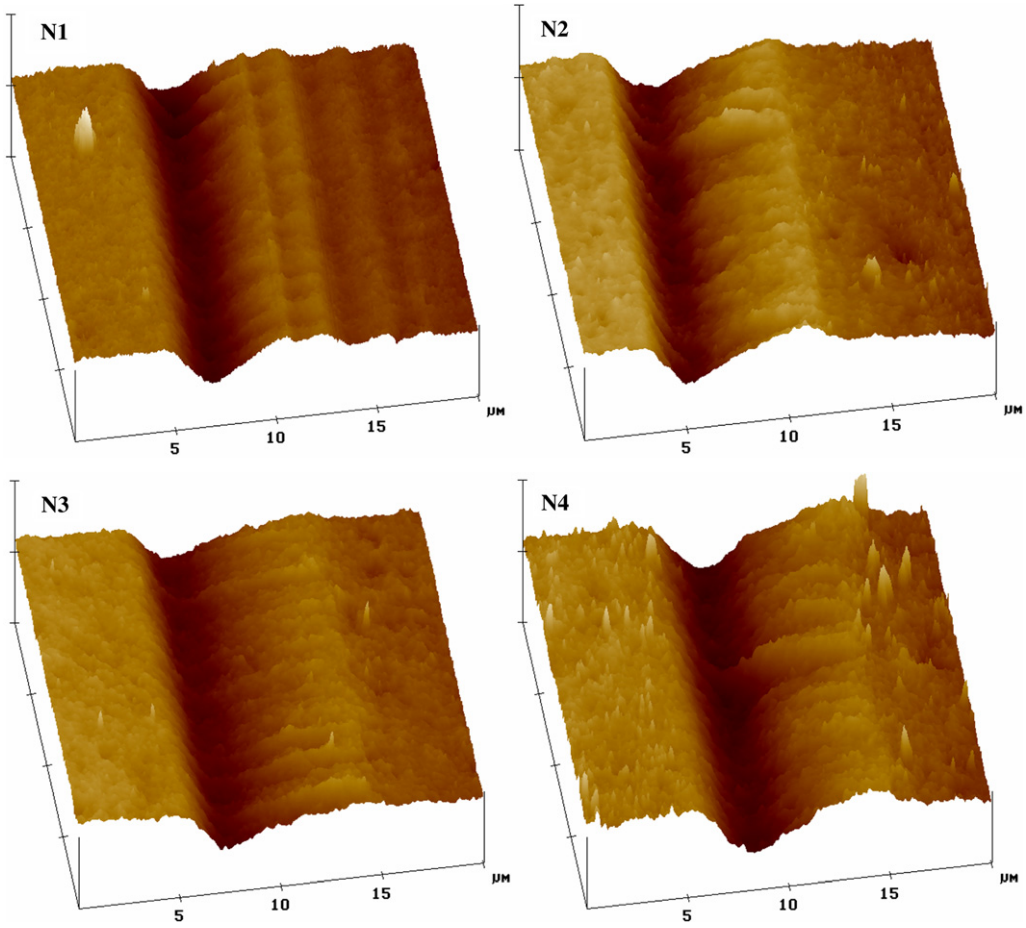

Fig. 3. 3-D AFM micrographs showing differences in nanoscratch deformation behaviors of nylon 66/organoclay/SEBS-g-MA ternary nanocomposites at a 20×20 μm field of view.

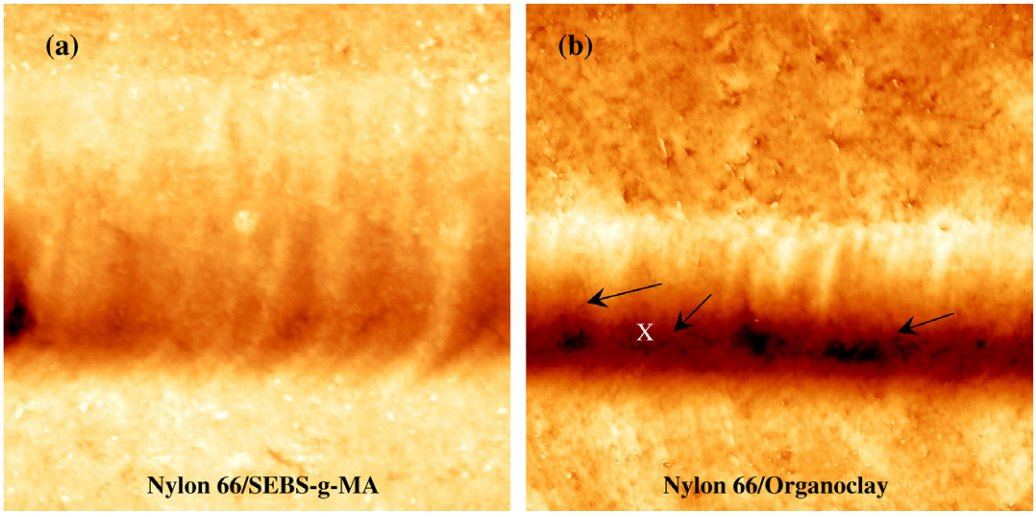

Fig. 4. 2-D AFM micrographs showing differences in the nanoscratch deformation behavior of two binary nanocomposites (nylon 66/SEBS-g-MA and nylon 66/organoclay) at a 20×20 μm field of view. The arrows indicate brittle cracks in the nylon/clay system.

region of the scratched subsurface these stresses may also lead to debonding between phases and cracking.

Apart from the negligible differences in the topographical features of the nanoscratched ternary nanocomposites, there is a clear distinction in the scratch residual depth (which is indicative of the specific nanowear rate) as measured by AFM (N1: 250 ± 9 nm, N2: 300 ± 10 nm, N3: 210 ± 7 nm, N4: 365 ± 11 nm). N3, which has the highest amount of exfoliated clay in nylon 66 matrix rather than in the SEBS-g-MA particles, shows the lowest scratch residual depth. In contrast, N4, which has the least amount of clay in the continuous nylon 66 matrix, has the largest scratch penetration. This indicates that to maximize the nanoscratch resistance, it is far more effective to have the exfoliated clay embedded in the continuous nylon 66 matrix phase rather than in the dispersed soft rubber domains. In addition, even though N1 and N2 have similar microstructures, different penetration depths can be attributed to the blending protocol employed. In N2, a two-step blending protocol is employed to prepare the final nanocomposite, whereas N1 is fabricated by a one-step extrusion process. Analogous to this behavior, N1 and N2 also showed differences in fracture behavior despite their similar microstructures [43].

However, a critical question may be raised about the use of ternary nanocomposites instead of binary nanocomposites, especially nylon 66/clay nanocomposites, in which the finely dispersed clay has a strong constraining effect on the matrix chains. The purpose of adding both a stiffener and a toughener to the polymer matrix can be easily understood if the nanoscratch morphologies of the binary nanocomposites (nylon 66/organoclay and nylon 66/SEBS-g-MA) are revealed and compared. Fig. 4 shows two-dimensional AFM micrographs of the binary nanocomposites. Enhanced plastic flow and pronounced grooves associated with the nanoscratch (penetration depth $\sim 390 \pm 19$ nm) can be found in the soft SEBS-g-MA/nylon 66 blend. In contrast, brittle cracks occur during nanoscratching of nylon 66/clay nanocomposite even though the penetration depth ($\sim 240 \pm 8$ nm) is comparable to that found in N1 and N3 ternary nanocomposites and other features, and mechanisms such as the presence of repeated, periodic plastically torn materials on the sides of the groove within the scratch tracks are similar to those found in all the ternary nanocomposites. These cracks may be formed as a result of the higher tensile stresses behind the indenter in this stiff nanocomposite (see below). Thus, it may be inferred that the lower degree of plastic flow in the ternary nanocomposites is due to the presence of a stiff phase, such as clay; while the resistance to brittle cracks is caused by the presence of the soft phase, i.e. SEBS-g-MA.

In addition, TEM (of the cross-section beneath the scratch track) is used to identify probable reasons for the brittle cracks observed in B1 (nylon 66/clay binary nanocomposite) and to clarify whether the cracks are only formed on the surface (as seen in Fig. 4) or underneath the scratch track. Fig. 5 shows TEM micrographs of the subsurface material beneath the scratch track in B1 caused by an applied load of 1 mN and a scratch velocity of 1 μm s^{-1} (taken from location 'X' in Fig. 4 from a plane normal to the sliding direction). Submicron and nanocracks associated with the clay layers up to 500 nm below the track are clearly seen. The high-magnification micrograph also shows that these fine cracks are formed between clay layers. When the sample is scratched by an indenter under an applied normal load, the maximum tensile stress is on the surface just behind the indenter. It has previously been suggested, based on the Hamilton–Goodman scratch model [50], that the higher maximum tensile stress on the surface of higher-modulus polymers may lead to the formation of surface cracks, cavitation and debonding between phases of multiphase polymers [51]. Further, the debonding between phases and cracking may be easily generated by internal sliding friction in the shear-stress dominant

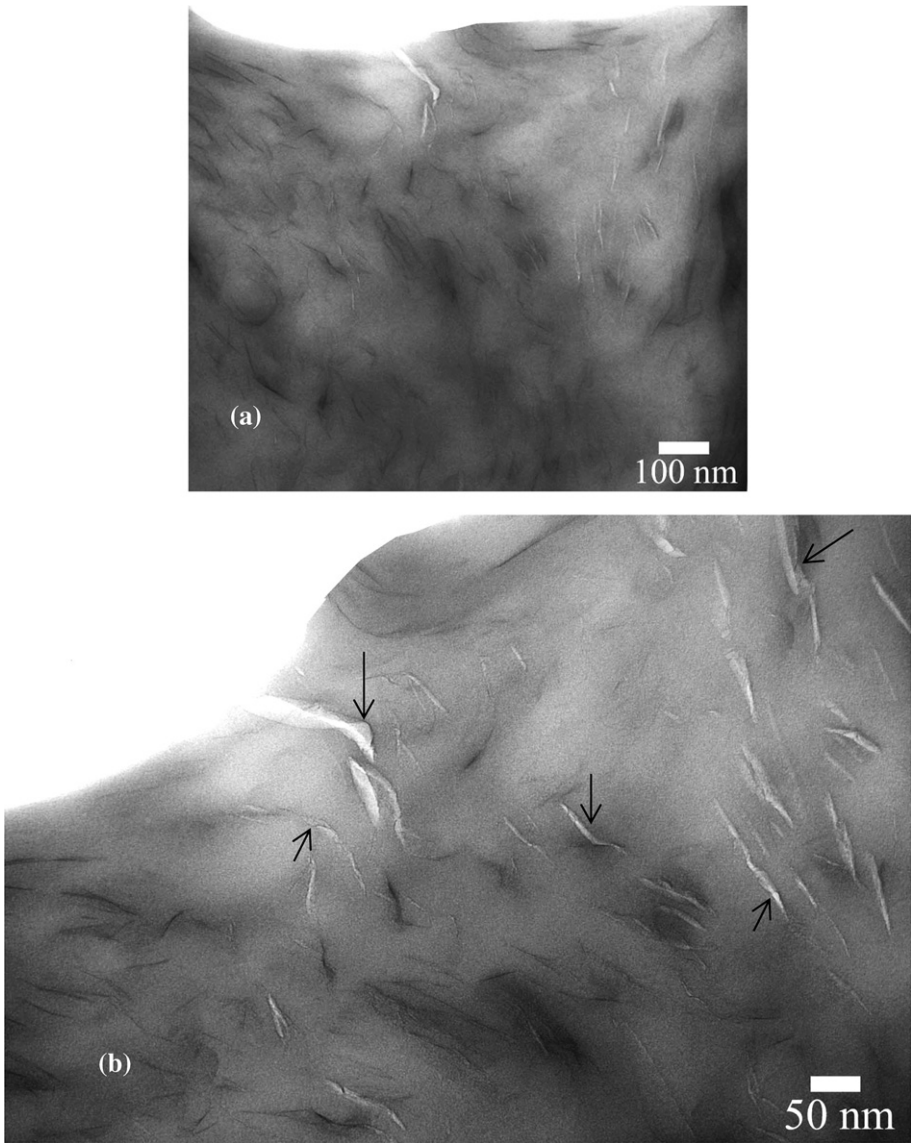

Fig. 5. TEM micrographs at two magnifications (a, b) of the subsurface damage beneath the scratch track in B1 (taken from location "X" along a plane normal to the sliding direction in Fig. 4) tested at an applied load of 1 mN and a scratch velocity of 1 μm s^{-1}. Arrows indicate nanocracks, which are associated with delaminations between the clay layers and the scratch track extends along the *x*, *y*-plane away from the top in (a).

region of the scratch subsurface. Compared to a single-pass scratch, under repeated sliding conditions, it is believed that the subsurface damage may extend and detach to form wear debris. In the present case, because of the weak electrostatic interactions between the clay interlayers, intra-gallery delaminations of preferentially oriented clay platelets occur, and nanocracks are formed under the prevalent stress conditions. In Fig. 5, a submicron edge crack at the surface of the scratch appears to almost link up with an adjacent subsurface crack. This gives the impression that the crack growth is normal to the surface, which is due to the fact that the planar dimensions of the delaminated platelets are along the sliding direction. This is unlike the case of 'delamination wear' where the cracks are nucleated below the surface and propagate parallel to – rather than perpendicular to – the surface under repeated sliding. In addition, as shown in Table 2, the average thickness of the clay particles present in B1 is ~1.9 nm, which indicates that on average only a couple of clay platelets may be present in each particle. But there is still a noticeable amount of delamination from the intra-gallery of the clay platelets. It is important to mention that the submicron and nanocracks observed here are not artefacts of the microtoming process. To ensure that the results were indeed typical of the scratch damage process, unscratched specimens were also microtomed and observed under similar conditions; it was confirmed that no such cracks were present [42]. Also, it should be noted that the cutting speed used for sectioning these materials was very low (0.2 mm s^{-1}), a sharp diamond knife was preferred to a glass knife, and microtoming was performed at cryo-conditions to avoid any sort of plastic deformation.

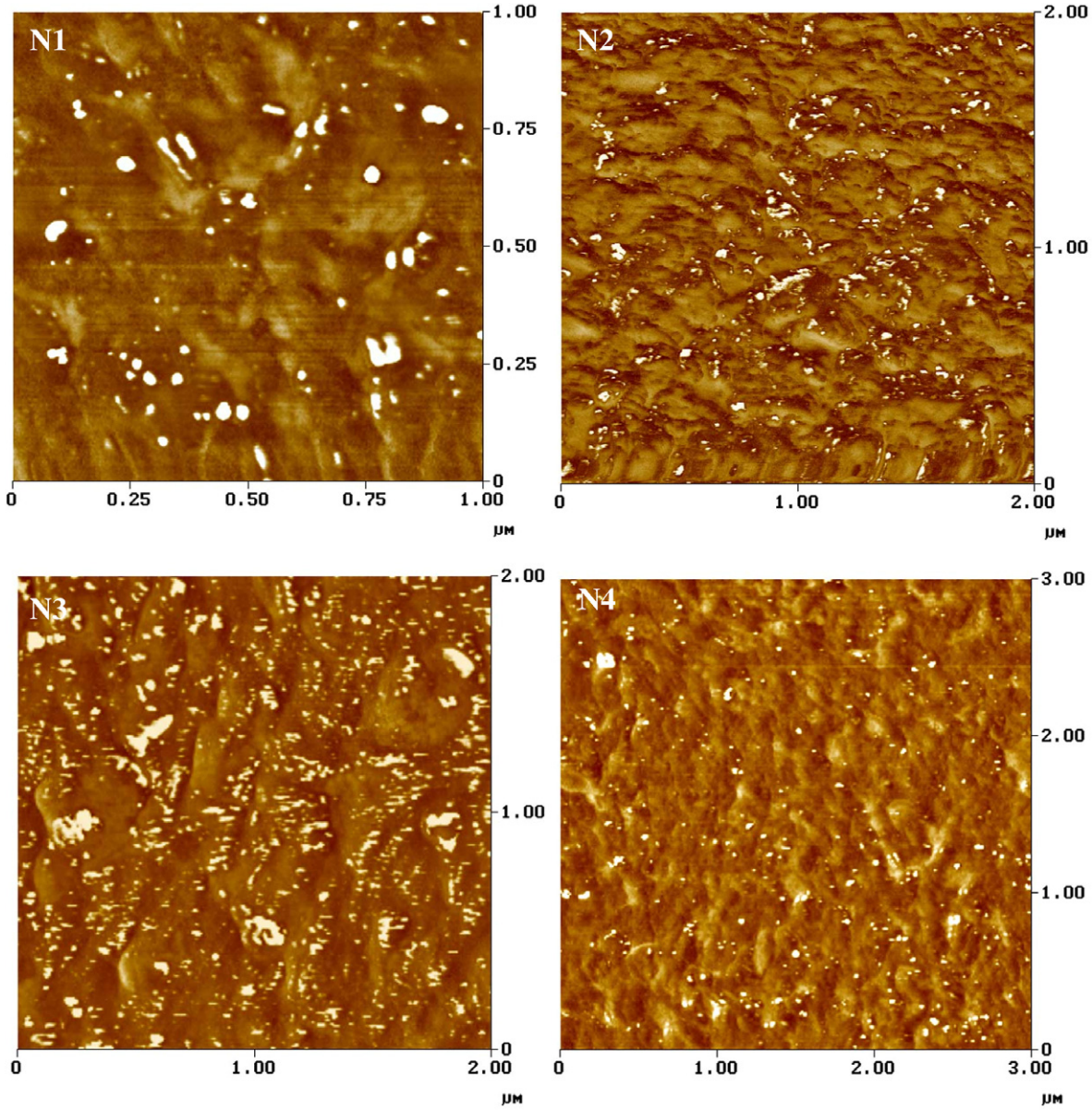

Fig. 6. 2-D AFM phase images showing differences in void formation during nanoscratch deformation of N1–N4. The dark phase represents the SEBS-g-MA and the continuous bright phase is nylon 66. Note the differences in the field of view.

3.2.3. Phase morphology

To understand the above results of scratch penetration and coefficient of friction in N1–N4 (i.e. higher frictional coefficients corresponding to lower penetration depths and vice versa), phase and amplitude (not shown here) AFM imaging was conducted on the scratched surfaces in all four polymer nanocomposites. 2-D phase AFM micrographs at different fields of view are shown in Fig. 6 for N1–N4. The dark zones are the soft SEBS-g-MA phase and the light, continuous phase is nylon 66 matrix. The interface of SEBS-g-MA and nylon 66 observed in the phase AFM images is not sharp because, as shown by Wu [52], the interfacial zone for grafted rubber and nylon matrix is about 50 nm. It seems that different extents of void formation are present in different materials (N1–N4) in the scratch damage region even at the light load (1 mN) and low speed (1 μm s^{-1}) applied here. In comparison to binary nylon 66/clay nanocomposite (B1) where brittle cracks are seen in the scratch track, in these ternary nanocomposites, although cracks cannot be found, nano- to submicron voids are, however, observed on the surfaces. These voids occur preferentially in the dispersed soft nanodomains of the SEBS-g-MA (dark zones) and are very different in size in all four nanocomposites.

The voids in Fig. 6 all occur on the surface of the scratch and may be caused by: (a) debonding of clay from matrix or SEBS-g-MA particles, (b) debonding of SEBS-g-MA particles from matrix or (c) cavitation of SEBS-g-MA dispersed particles. The predominant mechanism depends on the critical stress required and the material. It is noted that many more voids are seen in N3 and fewer in N4, with N1 and N2 in between. These observations are consistent with

the different frictions recorded in Fig. 2. That is, more friction work is dissipated to create more voids, such as in N3, which may be mainly due to mechanisms (b) and (c). In N1, N2 and N4, the voids are formed due to one of three mechanisms (a), (b) and (c). However, it is very difficult to clearly recognize the exact mechanisms responsible for the formation of voids from the AFM phase images shown here as it is difficult to identify the nanoclay layers at this field of view; furthermore, it is not appropriate to try and distinguish ~1.9 nm thick nanoclay layers with a tip ~100 times bigger than the thickness of clay layers.

Post-mortem TEM analysis has been conducted on cross-sections beneath the scratch track on N3 and N4 in order to better understand the damage induced by scratching, since they represent the two extremes of voids formed. Figs. 7 and 8 identify the subsurface damage in N3 and N4, respectively, showing clear differences due to the effect of microstructure of the nanocomposites. In N3, clay is least present in the rubber particles and so the rubber stiffness is unaffected. Thus, those rubber particles close to the scratched track experiences severe stretching, leading to rubber/matrix debonding or rubber cavitation (Fig. 7). However, the exfoliated clay in the nylon matrix enhances the resistance to scratch deformation as indicated by this material having the smallest scratch depth. Conversely, in N4, the absence of clay in the matrix makes it easier to deform plastically under the indenter with the largest scratch depth. The rubber particles stiffened by the intercalated clay are less able to deform or cavitate. However, debonding of clay from rubber particles can be seen in Fig. 8(b), indicating the weak bonding strength between intercalated clay and rubber. Also, the intercalated clay

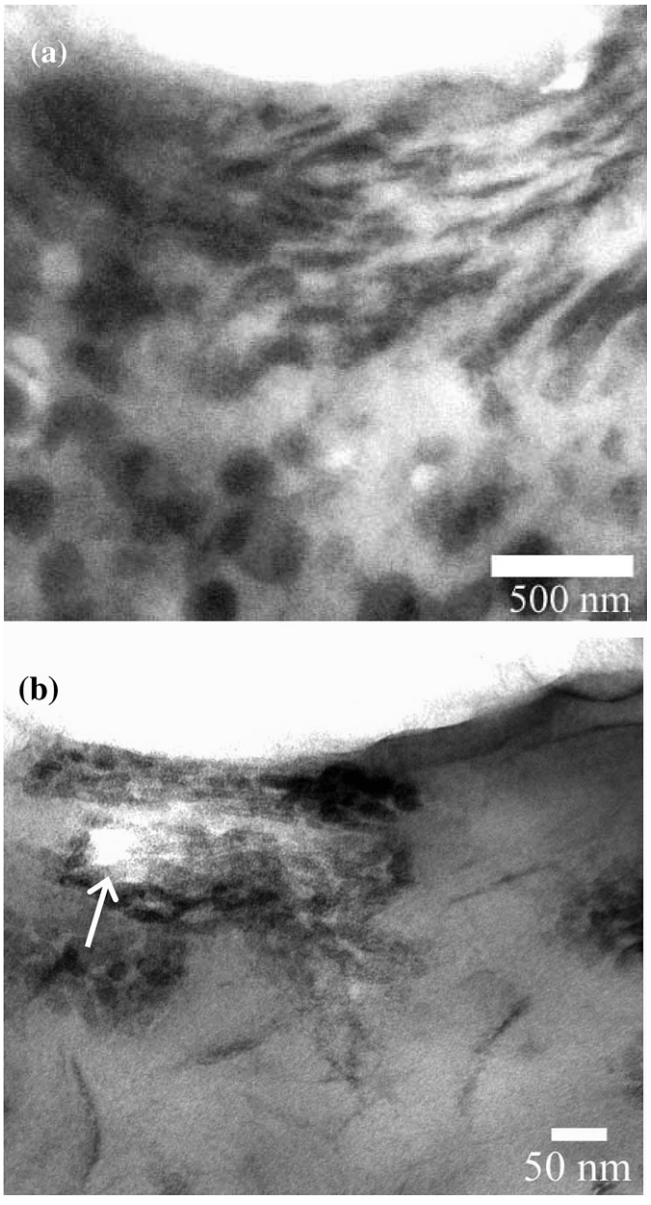

Fig. 7. TEM micrographs at two magnifications (a, b) of subsurface damage beneath the scratch track in N3 tested at an applied load of 1 mN and a scratch velocity of 1 μm s^{-1}. The arrow indicates the cavitation of SEBS-g-MA particles. The scratch track extends along the *x*, *y*-plane away from the top in (a).

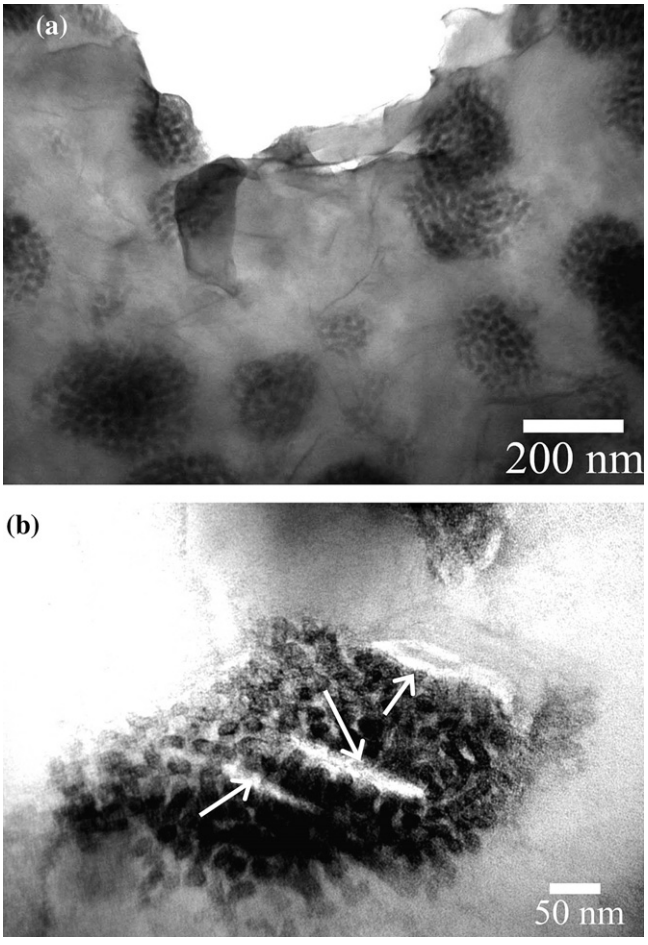

Fig. 8. TEM micrographs at two magnifications (a, b) of subsurface damage beneath the scratch track in N4 tested at an applied load of 1 mN and a scratch velocity of 1 μm s^{-1}. Debonding of intercalated clay in the matrix, along the particle–matrix interface and within the particles are observed (indicated by arrows). The scratch track extends along the *x*, *y*-plane away from the top in (a).

may delaminate under the moving indenter load as shown in Fig. 8(a).

From the above results and observations on scratch damage, it is evident that: (i) the location of the stiff clay layers determines the ultimate nanoscratch resistance (residual penetration depth) of the polymer nanocomposites, i.e. clay with a stabilized, exfoliated structure in the nylon matrix constrains the matrix chains, thus reducing the penetration depth; and (ii) compatibility of the different additives with the matrix and amongst each other is necessary to protect the integrity of the surface quality by minimizing the debonding of clay from rubber or delamination of intercalated clay during scratch damage. Thus, of the ternary nanocomposites, N3 has the best microstructure in terms of resistance to nanoscratch penetration and impact strength (Table 1). Unfortunately, such a material is not desirable for practical applications because it has a higher friction coefficient and the scratch damage is the most severe with many submicron voids despite its lower scratch penetration depth. For such purposes, it seems N4 or just pure nylon, N0, can in fact be a better option even though these materials have higher scratch penetration depths.

3.3. Nanoindentation

To corroborate the above results, nanoindentations of the four ternary nanocomposites were conducted at low loads of 1 and 5 mN using the same Berkovich indenter under similar testing conditions as nanoscratching. Typical loading-hold-unloading vs. displacement curves are shown in Fig. 9 at 5 mN, and further support the observations reported in Section 3.2. As a noticeable amount of creep strain at the peak load is observed for all the samples, holding (60 s) at the peak load is maintained to allow for dissipation of creep displacement and not affect the unloading curves. The hold period has to be long enough to completely account for the creep, i.e. towards the end of hold period the depth should be constant or the increase in depth with time negligible. In the present study, the increase in depths towards the end of hold period for all the ternary nanocomposites is in the range of ~0.07–0.3 nm. The standard deviations given in Fig. 9 are for five tests plotted against the mean curves. To avoid confusions due to overlapping of the standard deviations during the hold period, these are not shown. The unloading data are fitted to a power law function, as proposed by Oliver and Pharr [18], to determine the hardness and modulus, which are given in Table 1. The results clearly show that N3 has the highest hardness and elastic modulus of the remaining composites, hence emphasizing the importance of its microstructure. Also, the elastic modulus values obtained from nanoindentation are lower than those measured from conventional tensile testing. Similar observations were also reported in other polymer systems [11–13]. One of the possible origins for this discrepancy may be the different

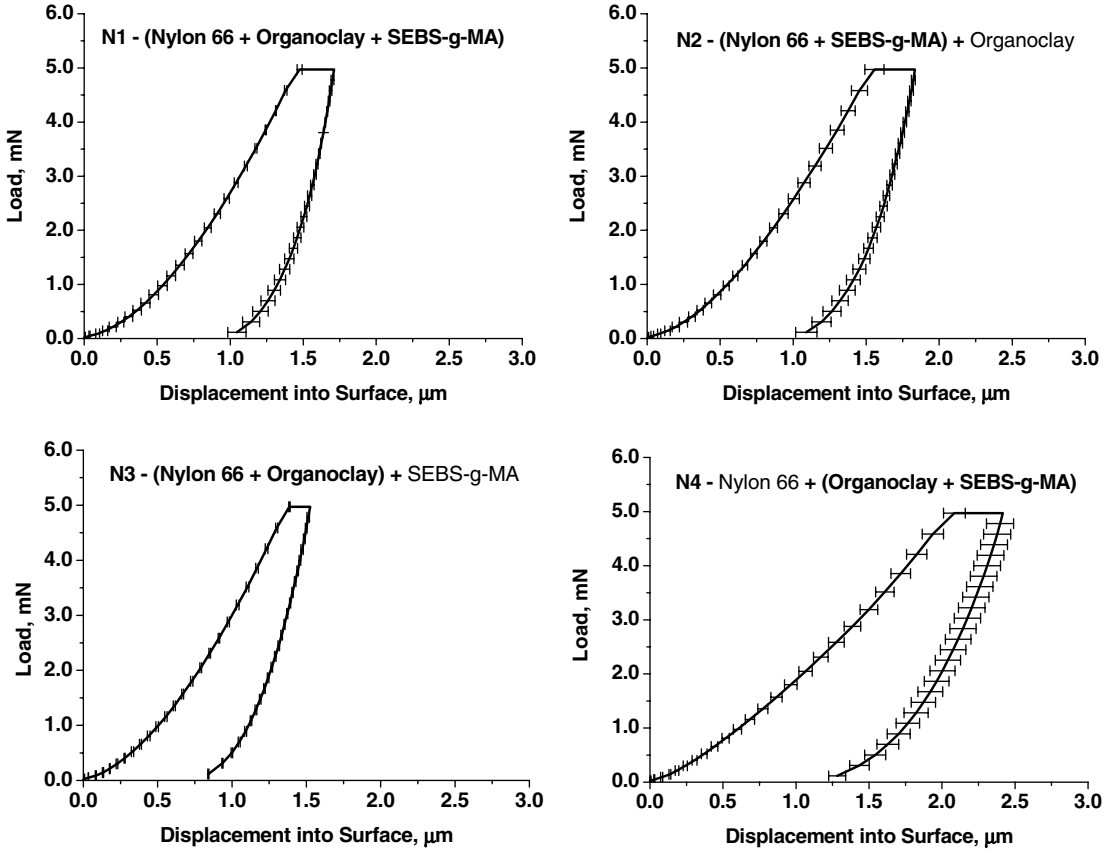

Fig. 9. Loading-hold-unloading curves showing nanoscale differences in N1–N4.

loading directions used for these measurements. Elastic modulus is measured along the injection molding direction in a tensile test where the polymer chains are expected to align or orient in that direction; but normal to the injection molding direction during nanoindentation. Further, in clay-filled polymers, the orientation of clay with respect to the loading conditions affects the measured values. Another factor that may play a role is the local crystallinity (important in nanoindentation) vs. bulk crystallinity (determining factor in tensile testing) of a polymer.

4. Implications and conclusions

Many past studies have suggested that for superior nanoscratch resistance, polymers with higher modulus are preferred [22,51]. The present study, however, shows that when dealing with polymer nanocomposites, modulus is not the only factor that should be considered. Instead, an in-depth understanding of all microstructural parameters and their response to nanoscratch must be evaluated. Detailed illustrations of the deformation and damage behavior that accompanies the nanoscratch process have been presented with the aid of AFM and TEM. These observations have extended our current knowledge of the role of nanoscale additives. In particular, the role played by the nanoscale domains in the present composites in determining the formation of surface brittle cracks or nanovoids even at low load and speed is critical to the ultimate performance of the material. Nevertheless, the scratch penetration depth (200–400 nm) in the present work is still on the high side. It is hence necessary to further reduce the penetration depth by varying the applied load, sliding speed or indenter geometry so that the scratch track is less than or within the same size range as the nano-additives in order to identify the real ''nano-effect''.

Acknowledgements

We would like to thank the Australian Research Council (ARC) for continuing support of this project on ''Polymer Nanocomposites''. Y.-W.M. and Z.-Z.Y. are, respectively, an Australian Federation Fellow and an Australian Post-doctoral Fellow supported by the ARC and tenable at the University of Sydney. A.D. also thanks the Australian Government for an International Postgraduate Research Scholarship Award and the University of Sydney for an International Postgraduate Award to undertake a PhD program in the CAMT.

References

[1] Briscoe BJ, Sebastian KS, Adams MJ. J Phys D: Appl Phys 1994;27:1.
[2] VanLandingham MR, Villarrubia JS, Guthrie WF, Meyers GF. Macromol Symp 2001;167:15.
[3] Penumadu D, Dutta A, Pharr GM, Files B. J Mater Res 2003;18:1849.
[4] Flores A, Calleja FJB. Philos Mag A 1998;78:1283.
[5] Fang TH, Chang WJ. Microelectron J 2004;35:595.
[6] Beake BD, Goodes SR, Smith JF. J Mater Res 2004;19:237.
[7] Park K, Mishra S, Lewis G, Losby J, Fan Z, Park JB. Biomaterials 2004;25:2427.
[8] Hochstetter G, Jimenez A, Cano JP, Felder E. Tribol Int 2003;36:973.
[9] Drechsler D, Karbach A, Fuchs H. Appl Phys A 1998;66:S825.
[10] Beake BD, Chen S, Hull JB, Gao F. J Nanosci Nanotechnol 2002;2:73.
[11] Shen L, Phang IY, Chen L, Liu T, Zeng K. Polymer 2004;45:3341.
[12] Shen L, Phang IY, Liu T, Zeng K. Polymer 2004;45:8221.
[13] Phang IY, Liu T, Mohamed A, Pramoda KP, Chen L, Shen L, et al. Polym Int 2005;54:456.
[14] Li X, Gao H, Scrivens WA, Fei D, Xu X, Sutton MA, et al. Nanotechnology 2004;15:1416.
[15] Liu T, Phang IY, Shen L, Chow SY, Zhang WD. Macromolecules 2004;37:7214.
[16] Nai MH, Lim CT, Zeng KY, Tan VBC. J Metastab Nanocryst Mater 2005;23:363.
[17] Xu GC, Li AY, Zhang LD, Yu XY, Xie T, Wu GS. J Reinf Plast Comp 2004;23:1365.
[18] Oliver WC, Pharr GM. J Mater Res 1992;7:1564.
[19] Bhushan B. Handbook of micro/nanotribology, vol. 2. Boca Roton (FL): CRC Press; 1999.
[20] Bhushan B. Wear 1999;225–229:465.
[21] Bhushan B, Israelachvilli JN, Landman U. Nature 1995;374:607.
[22] Wong JSS, Sue H-J, Zeng KY, Li RKY, Mai Y-W. Acta Mater 2004;52:431.
[23] Kim JK, Hodzic A. J Adhes 2003;79:383.
[24] Overney RM. TRIP 1995;3:359.
[25] Han Y, Schmitt S, Friedrich K. Appl Comput Mater 1999;6:1.
[26] Kim JK, Sham ML, Wu J. Composites A 2001;32:607.
[27] Hodzic A, Stachurski ZH, Kim JK. Polymer 2000;41:6895.
[28] Baljon ARC, Robbins MO. MRS Bull 1997;22:22.
[29] Steinmann PA, Tardy Y, Hintermann HE. Thin Solid Films 1987;154:333.
[30] Wang HF, Nelson JC, Gerberich WW, Deve HE. Acta Metall Mater 1993;42:695.
[31] Bhushan B, Koinkar VN. Appl Phys Lett 1994;64:1653.
[32] Li T, Chen Q, Schadler LS, Siegel RW. Polym Comp 2002;23:1076.
[33] Ng CB, Schadler LS, Siegel RW. Nanostruct Mater 1999;12:507.
[34] Petrovicova E, Knight R, Schadler LS, Twardowski T. J Appl Polym Sci 2001;78:2272.
[35] Kietzke T, Neher D, Landfester K, Montenegro R, Guntner R, Scherf U. Nat Mater 2003;2:408.
[36] Wetzel B, Haupert F, Zhang MQ. Comp Sci Technol 2003;63:2055.
[37] Zhang MQ, Rong MZ, Yu SL, Wetzel B, Friedrich K. Wear 2002;253:1086.
[38] Xing XS, Li RKY. Wear 2004;256:21.
[39] Chang L, Zhang Z, Breidt C, Friedrich K. Wear 2005;258:141.
[40] Friedrich K. In: Friedrich K, editor. Advances in Composite Tribology. Amsterdam: Elsevier; 1993. p. 209.
[41] Dasari A, Yu Z-Z, Mai Y-W. Polymer 2005;46:5986.
[42] Dasari A, Yu Z-Z, Yang M, Zhang QX, Xie XL, Mai Y-W. Compos Sci Technol 2006;66:3097.
[43] Dasari A, Yu Z-Z, Mai Y-W, Yang M. in preparation.
[44] Okada O, Keskkula H, Paul DR. J Polym Sci Part B: Polym Phys 2004;42:1739.
[45] Landman U, Luedtke WD, Gao J. Langmuir 1996;12:4514.
[46] Tang H, Martin DC. J Mater Sci 2003;38:803.
[47] Briscoe BJ. Tribol Int 1998;31:121.
[48] Briscoe BJ, Pelillo E, Sinha SK. Polym Eng Sci 1996;36:2996.
[49] Adams MJ. Wear 2001;251:1579.
[50] Hamilton GM, Goodman LE. J Appl Mech 1966;33:371.
[51] Xiang C, Sue H-J, Chu J, Coleman B. J Poly Sci Part B: Poly Phys 2001;39:47.
[52] Wu S. Polymer 1985;26:1855.